



**HAL**  
open science

# The effect of thermal pressurization on dynamic fault branching

Yumi Urata, Sébastien Hok, Eiichi Fukuyama, Raul Madariaga

► **To cite this version:**

Yumi Urata, Sébastien Hok, Eiichi Fukuyama, Raul Madariaga. The effect of thermal pressurization on dynamic fault branching. *Geophysical Journal International*, 2014, 196 (issue 2), p. 1237-1246. 10.1093/gji/ggt457 . irsn-01314626

**HAL Id: irsn-01314626**

**<https://irsn.hal.science/irsn-01314626>**

Submitted on 17 Jun 2021

**HAL** is a multi-disciplinary open access archive for the deposit and dissemination of scientific research documents, whether they are published or not. The documents may come from teaching and research institutions in France or abroad, or from public or private research centers.

L'archive ouverte pluridisciplinaire **HAL**, est destinée au dépôt et à la diffusion de documents scientifiques de niveau recherche, publiés ou non, émanant des établissements d'enseignement et de recherche français ou étrangers, des laboratoires publics ou privés.

# The effect of thermal pressurization on dynamic fault branching

Yumi Urata,<sup>1</sup> Sébastien Hok,<sup>2</sup> Eiichi Fukuyama<sup>1</sup> and Raúl Madariaga<sup>3</sup>

<sup>1</sup>National Research Institute for Earth Science and Disaster Prevention, Tsukuba, Ibaraki 305-0006, Japan. E-mail: [urata@bosai.go.jp](mailto:urata@bosai.go.jp)

<sup>2</sup>Institut de Radioprotection et de Sûreté Nucléaire (IRSN), PRP-DGE, SCAN, BERSIN, Fontenay-aux-Roses, France

<sup>3</sup>Laboratoire de Géologie, UMR 8538, CNRS, École Normale Supérieure, Paris, France

Accepted 2013 November 6. Received 2013 September 25; in original form 2013 May 14

## SUMMARY

We numerically investigate the effect of thermal pressurization (TP) on fault branch behaviour during dynamic rupture propagation, a situation likely to occur during large earthquakes at subduction interfaces. We consider a 2-D mode II (in-plane) rupture in an infinite medium that propagates spontaneously along a planar main fault and encounters an intersection with a pre-existing branching fault. The fault system is subjected to uniform external stresses. We adopt the values used by Kame *et al.* We use the 2-D boundary integral equation method and the slip-weakening friction law with a Coulomb failure criterion, allowing the effective normal stress to vary as pore pressure changes due to TP. We reveal that TP can alter rupture propagation paths when the dip angle of the main fault is small. The rupture propagation paths depend on the branching angle when TP is not in effect on either of the faults, as described by Kame *et al.* However, the dynamic rupture processes are controlled more by TP than by the branching angle. When TP is in effect on the main fault only, the rupture propagates along the main fault. It propagates along the branch when TP is in effect on both faults. Finally, we considered the case where there is a free surface above the branch fault system. In this case, the rupture can propagate along both faults because of interaction between the free surface and the branch fault, in addition to TP on the main fault.

**Key words:** Earthquake dynamics; Computational seismology; Dynamics and mechanics of faulting; Fractures and faults; Mechanics, theory, and modelling.

## 1 INTRODUCTION

One important issue with regard to future large earthquakes is the assessment of strong ground motions and tsunamis. To accurately evaluate seismic and tsunami hazards, we must have a fundamental understanding of the physics of the dynamic rupture propagation along faults with complex geometry because, as geological and seismic observations have indicated, large earthquakes generally occur on complex fault systems including jogs, step-overs, bends and branches rather than a single planar fault (e.g. Sibson 1986; Wesnousky 1988; Sieh *et al.* 1993). Here, we focus on fault branching. Branch faults have been observed in shallow inland strike-slip earthquakes (e.g. Archuleta 1984; Aochi & Fukuyama 2002). Recently, branch faults have also been observed along subduction interfaces at shallow depths by seismic reflection surveys, such as in the Nankai subduction zone off southwest Japan (e.g. Park *et al.* 2002; Moore *et al.* 2007), in the Japan Trench (Tsuji *et al.* 2013), and in the north Ecuador–south Colombia oceanic margin (Collot *et al.* 2008).

Rupture propagation on branch fault systems has been studied both theoretically and numerically. Theoretical analyses suggested that rupture velocity and pre-stress states control rupture paths (Poliakov *et al.* 2002). These features have also been investigated

using numerical simulations. Kame *et al.* (2003) performed many numerical simulations of 2-D mode II ruptures in an infinite elastic medium. They showed that rupture propagation paths are controlled by the inclination of the maximum principal stress, the branching angle, and incoming rupture velocity at the branching intersection. In addition, Bhat *et al.* (2007) suggested that the finite length of the branching fault could affect the rupture dynamics. Numerical models of earthquake ruptures including branch faults have mainly focused on strike-slip events (Aochi & Fukuyama 2002; Oglesby *et al.* 2003; Bhat *et al.* 2004; Fukuyama & Mikumo 2006). To model a megathrust earthquake rupture, Tamura & Ide (2011) introduced material heterogeneity and a free surface. They considered a spontaneously propagating mode II crack on a bi-material interface and a branching fault, suggesting that material contrast plays an important role in dynamic fault branching.

In subduction zones, the existence of fluid has been suggested (e.g. Hasegawa *et al.* 2009), and fluid at the plate interface is thought to play an important role during rupture propagation. As one possible effect of the fluid's presence, Sibson (1973, 1977) proposed thermal pressurization (TP), an increase in pore fluid pressure due to frictional heating in wet conditions, that results in a decrease in effective normal stress. Field observations and rock experiments have suggested that TP can be in effect during earthquakes. Ishikawa *et al.*

(2008) analysed the compositions of major and trace elements and isotope ratios of borehole core samples from the Chelungpu fault, Taiwan, and suggested the coseismic presence of high-temperature fluids ( $>350^\circ\text{C}$ ). They mentioned that TP may have been in effect during the  $M_w$  7.6 1999 Chi-Chi earthquake because the fault's hydraulic diffusivity was estimated to be low (Doan *et al.* 2006). Ujiie *et al.* (2007) studied the ancient subduction thrust faults in the Shimanto accretionary complex of southwest Japan and observed that the ultracataclasite layer indicates that granular material was injected into the adjacent wall rocks. They suggested that the injected material represents fluidization during a seismic slip and that TP appears to be, of the various fluidization mechanisms, the most consistent with their observations. Ujiie & Tsutsumi (2010) conducted high-velocity friction experiments on clay-rich fault gouge obtained from the megasplay fault zone in the Nankai subduction zone. They observed a rapid increase in the gouge's temperature during rapid slip weakening under wet conditions, which implies that rapid weakening results from TP.

Numerical simulations suggested that TP can increase breakdown stress drop (e.g. Andrews 2002; Bizzarri & Cocco 2006b), peak slip rate and rupture velocity (Bizzarri & Cocco 2006a; Bizzarri & Spudich 2008; Urata *et al.* 2008). As a result of these effects, TP also affects rupture processes when geometric complexities, such as step-overs, are taken into consideration (Urata *et al.* 2012). TP can also modify fault behaviour at longer timescales. Noda & Lapusta (2013) proposed a model applicable for the  $M_w$  9.0 2011 Tohoku-Oki earthquake in which a creeping unlocked part of the fault can become an unstable seismically slipping patch due to TP's effects. Their model for the time of the earthquake produced higher slip but a smoother slip-rate history in the part of the fault where TP was active, making the model qualitatively consistent with seismic observations. It should be noted that they considered a single fault plane without geometrical complexity and did not consider the free surface. As far as we know, the geometry of shallow thrust faults has never been considered in dynamic rupture simulations with TP, although such geometry is common in subduction zones (e.g. Park *et al.* 2002; Moore *et al.* 2007; Collot *et al.* 2008; Tsuji *et al.* 2013).

As mentioned above, TP could affect dynamic fault branching phenomena strongly. However, previous studies on branching issues have not taken TP into account. The purpose of this study is to explore the effects of TP on dynamic fault branching. We also examine the effects of the free surface and TP simultaneously. We perform 2-D numerical simulations of spontaneous ruptures with TP, based on the branch fault model of Kame *et al.* (2003). The principal stresses, the inclination of the maximum principal stress with respect to the main fault, and the branching angle are the same as those of Kame *et al.* (2003). We also assume that the maximum principal stress axis is horizontal in cases with free surfaces (i.e. the maximum stress axis is parallel to the surface). We investigate whether the rupture propagates along the main and/or branch faults to demonstrate how TP alters dynamic fault branching. Finally, we simulate a case where there is a free surface above the branch fault system.

## 2 METHOD

### 2.1 Model

We consider a 2-D mode II (in-plane) rupture that propagates along a planar main fault and encounters an intersection with a pre-existing branch fault (Fig. 1). The branch fault makes an angle  $\theta$  with the

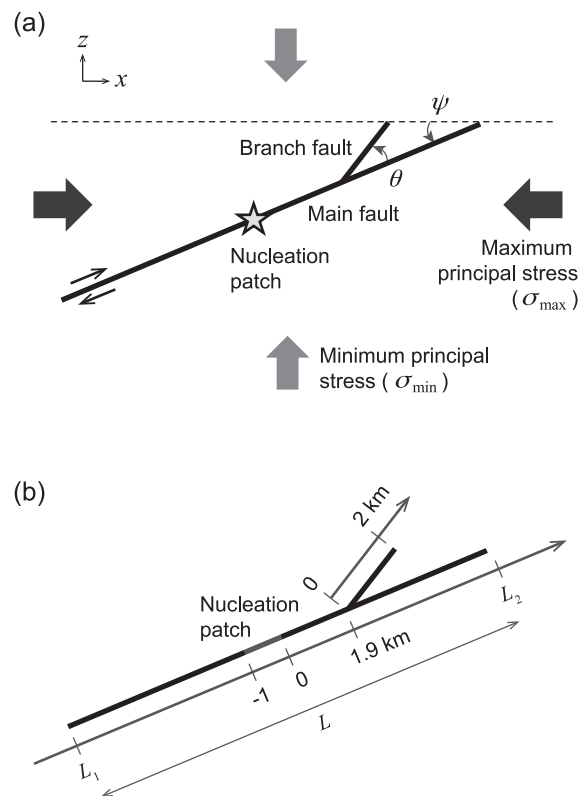


**Figure 1.** 3-D model used in this study. (a) The dashed line shows the free surface, which is considered only in Section 3.3. (b) The length of the main fault  $L$  depends on the values of  $\psi$  and  $\theta$ .

main fault. The fault system is in an infinite, homogenous, isotropic and linear elastic medium, subjected to uniform external stresses  $\sigma_{\max}$  and  $\sigma_{\min}$  (compression is taken as positive). The fault planes are on the  $xz$ -plane. The direction of  $\sigma_{\max}$  is parallel to the  $x$ -axis, and it makes an angle  $\psi$  with the main fault plane.

### 2.2 Numerical procedure for dynamic ruptures

The numerical algorithm for dynamic ruptures is based on the 2-D boundary integral equation method (BIEM) with integration kernels described by eq. (A1) of Tada & Madariaga (2001). These kernels link both in-plane shear slip (mode II) and opening slip (mode I) finite dislocation to stress tensor change in the medium surrounding the slipping crack, as functions of time. Please note that in this study, opening slip is set to zero for faults, and is computed for free surface elements as vertical displacement (see Appendix A). Our fault model consists of a collection of individual fault elements (any geometry consisting of a combination of small planar fault elements can be considered). Each of them has its own amount of dislocation at a given time step and thus its own contribution to the stress change in the surrounding medium, thanks to the integration kernels. The spontaneous rupture is obtained by solving the loading stress applied to each fault element at each time step together with the prescribed frictional behaviour as a function of its slip history (constitutive law).

A rupture is initiated by artificially adding shear stress in a small patch on the main fault (Fig. 1). It then proceeds spontaneously, governed by a slip-weakening law with the Coulomb failure criteria (Fig. 2; Ida 1972):

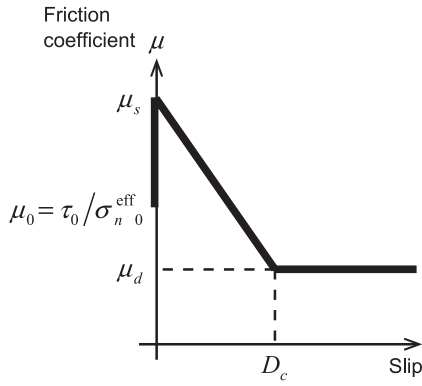


**Figure 2.** Slip-weakening fracture criterion. The initial coefficient of friction is  $\mu_0$ . Slip begins when the coefficient of friction reaches the static coefficient of friction  $\mu_s$ . The coefficient of friction decreases linearly to the dynamic coefficient of friction  $\mu_d$ . After the slip reaches the characteristic displacement  $D_c$ , the coefficient equals  $\mu_d$ .

$$\tau = \begin{cases} \mu_s \sigma_n^{\text{eff}} - (\mu_s \sigma_n^{\text{eff}} - \mu_d \sigma_n^{\text{eff}}) \Delta u / D_c & 0 \leq \Delta u < D_c \\ \mu_d \sigma_n^{\text{eff}} & \Delta u \geq D_c \end{cases}, \quad (1)$$

where  $\tau$  is the shear stress,  $\mu_s$  is the static coefficient of friction,  $\sigma_n^{\text{eff}}$  is the effective normal stress,  $\mu_d$  is the dynamic coefficient of friction,  $D_c$  is the characteristic displacement and  $\Delta u$  is the slip. The friction coefficients and  $D_c$  are assumed to be uniform and the same on the two faults.

### 2.3 Calculation of pore pressure change due to TP

We now consider the effect of frictional heating. Once slip is initiated and the slip rate increases, the pore fluid pressure  $p$  increases because of frictional heating. Then,  $\sigma_n^{\text{eff}}$  decreases according to the relation  $\sigma_n^{\text{eff}} = \sigma_n - p$ , where  $\sigma_n$  is the normal stress. We assume that the pore pressure change  $\Delta p$  at location  $\mathbf{x}$  on the fault surface due to TP obeys the following equation (Bizzarri & Cocco 2006a),

$$\Delta p(\mathbf{x}, t) = \frac{\gamma}{w} \int_0^{t-\varepsilon} dt' \cdot \left\{ -\frac{\chi}{\omega - \chi} \operatorname{erf} \left( \frac{w}{4\sqrt{\chi}(t-t')} \right) + \frac{\omega}{\omega - \chi} \operatorname{erf} \left( \frac{w}{4\sqrt{\omega}(t-t')} \right) \right\} \tau(\mathbf{x}, t') v(\mathbf{x}, t'), \quad (2)$$

where the dimensionless parameter  $\gamma$  is  $\alpha_f / \beta_f c$ ,  $w$  is the shear zone thickness,  $\chi$  is thermal diffusivity, hydraulic diffusivity  $\omega$  is  $k / \eta \beta_f \phi$ ,  $k$  is permeability,  $\phi$  is porosity,  $v$  is slip velocity,  $\varepsilon$  is an arbitrarily small positive real number and  $\operatorname{erf}(\cdot)$  is the error function defined below.

$$\operatorname{erf}(y) \equiv \frac{2}{\sqrt{\pi}} \int_0^y dx \cdot e^{-x^2}. \quad (3)$$

The definitions of  $\alpha_f$ ,  $\beta_f$ ,  $c$  and  $\eta$  are listed in Table 1. The assumptions in eq. (2) and their validity are set forth in Bizzarri & Cocco (2006a) and Urata *et al.* (2008).  $\omega$  and  $\phi$  are set to be constant. We assumed that fluid migration between the main and branch faults does not affect each other. We discuss the validity of this assumption in Section 4. Note that the yield stress values  $\tau_s = \mu_s \sigma_n^{\text{eff}}$  are not affected by TP because the pore pressure is constant ( $p = p_0$ ) before the rupture front arrives.

**Table 1.** Simulation parameters for thermal pressurization.

Property	Symbol	Value
Permeability	$k$	$5 \times 10^{-17} \text{ m}^2$
Porosity	$\phi$	0.025
Thermal diffusivity	$\chi$	$1 \times 10^{-6} \text{ m}^2 \text{ s}^{-1}$
Heat capacity	$c$	$3 \times 10^6 \text{ J (m}^3 \text{ K)}^{-1}$
Shear zone thickness	$w$	0.01 m
Thermal expansion of fluid <sup>a</sup>	$\alpha_f$	$6.589 \times 10^{-4} \text{ K}^{-1}$
Compressibility of fluid <sup>a</sup>	$\beta_f$	$4.332 \times 10^{-10} \text{ Pa}^{-1}$
Viscosity <sup>a</sup>	$\eta$	$3.224 \times 10^{-4} \text{ Pa s}$

<sup>a</sup>The values are obtained by using PROPATH (PROPATH Group 2008) with pressure of 30 MPa and temperature of 90 °C.

### 2.4 Validation tests

Before computing the dynamic fault branching with TP, we tested our numerical code. For dynamic rupture propagation with TP on one fault plane in an infinite medium, we compare the results with those of the 3-D finite-difference method (FDM) used by Urata *et al.* (2008). The initial stresses,  $\mu_s$ ,  $\mu_d$  and  $D_c$  are assumed uniform in the comparison. In the 3-D FDM calculations, we set the fault width along the  $y$ -direction long enough to stay in a pure 2-D regime and measured the slip evolution at  $y = 0$ , which we compared with that measured using the 2-D BIEM (Fig. 3a). Figs 3(b) and (c) show the propagation of the rupture front and the evolution of the slip velocity at the centre of the fault for the BIEM (red curves) and the FDM (black curves). In the simulations,  $\mu_s$ ,  $\mu_d$  and  $D_c$  are 0.74, 0.5 and 0.25 m, respectively. The initial effective normal stress  $\sigma_{n0}^{\text{eff}} = \sigma_{n0} - p_0$  and the initial shear stress  $\tau_0$  are 102 and 66 MPa, respectively. The FDM grid spacing ( $\Delta x$ ,  $\Delta y$  and  $\Delta z$ ) and time interval are 12.5 m and 0.001 s, respectively. The BIEM grid spacing  $\Delta x_1$  and time interval are 12.5 m and 0.0009 s, respectively. The density  $\rho$ ,  $P$ -wave velocity  $v_p$  and  $S$ -wave velocity  $v_s$  are 2670 kg m<sup>-3</sup>, 6.000 km s<sup>-1</sup> and 3.464 km s<sup>-1</sup>, respectively. The TP parameters are shown in Table 1. As shown in Figs 3(b) and (c), the red and black curves overlap; the solutions obtained by the BIEM and the FDM are almost identical. This comparison validates our calculation of dynamic rupture on a planar fault with TP.

To compare the distribution of off-fault stress changes, we first compute the stresses on the plane parallel to the fault (Fig. 3a). Fig. 4 shows the changes in the shear and normal stresses obtained

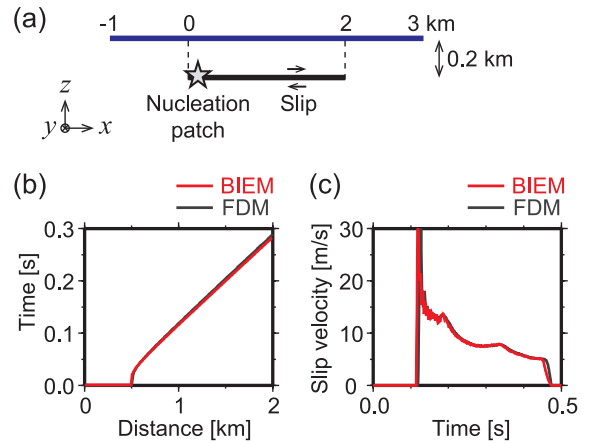


**Figure 3.** Comparison of dynamic rupture propagation with TP calculated by the BIEM and by the FDM. (a) Model configuration. The black line shows the fault plane. The blue line is referenced in Fig. 4. (b) Evolution of the rupture front. (c) Time histories of slip velocity at  $x = 1$  km. (b, c) Red and black curves indicate BIEM and FDM solutions, respectively.

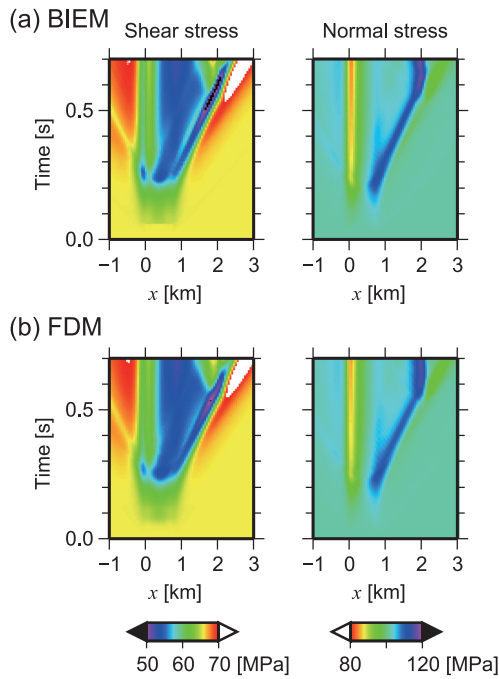


**Figure 4.** Comparison of off-fault stress changes calculated by the BIEM (a) and by the FDM (b). The left- and right-hand panels show the shear and normal stresses, respectively, on the plane indicated by the blue line in Fig. 3(a).

by the BIEM and the FDM. In these simulations, TP is not in effect and the computations are done in full space.  $\rho$ ,  $v_p$ ,  $v_s$ ,  $\mu_s$ ,  $\mu_d$  and  $D_c$  are the same as those used in Figs 3(b) and (c).  $\sigma_{n0}^{\text{eff}}$  and  $\tau_0$  for both the fault and off-fault planes are the same as those used in Figs 3(b) and (c). The FDM grid spacing and time interval are 50 m and 0.004 s, respectively. The BIEM grid spacing  $\Delta x_1$  and time interval are 50 m and 0.0036 s, respectively. The grid spacings and time intervals are long compared with the simulations in Figs 3(b) and (c), because TP is absent. The off-fault stress changes calculated by the two methods are quite similar (Fig. 4). We confirmed that our numerical code properly provides dynamic stress changes on an off-fault plane parallel to a fault plane.

We also tested the off-fault static stress change by comparing our results with those computed by the Okada's static deformation code (Okada 1992). To compute the off-fault static stress change tensor using the 2-D BIEM, we calculated the slip evolution on a fault in full space and measured the stress change after a sufficiently long time had passed. TP is not in effect in this computation. Since we only needed the final stress change, the initial stress on the fault is set higher than the static shear strength. The rupture initiated simultaneously all over the fault and slip evolved according to the slip-weakening law (eq. 1, Fig. 2). The fault length was 50 m.  $\sigma_{n0}^{\text{eff}}$ ,  $\tau_0$ ,  $\mu_s$ ,  $\mu_d$  and  $D_c$  were 100 MPa, 37 MPa, 0.36, 0.1 and 0.008 m, respectively.  $\rho$ ,  $v_p$  and  $v_s$  are the same as those used in Fig. 3. The grid spacing and the time interval were 12.5 m and 0.0009 s, respectively. In Okada's computation, which deals with finite rectangular sources in 3-D half-space, we put the fault width along the  $y$ -direction centred at  $y = 0$ . The fault width was set long enough to stay in a pure 2-D regime and the fault was located deep enough not to be affected by the free surface. The static stress change tensor was evaluated along the centre of the fault length (i.e.  $y = 0$ ). We then compared Okada's static stress change tensors and our BIEM computation and confirmed that they were identical.

This experiment certifies that our off-fault stress change tensors are correctly computed.

Finally, we compared our dynamic fault branching behaviour in the absence of TP with the results of Kame *et al.* (2003). We examined cases where the angles  $\psi$  between  $\sigma_{\text{max}}$  and the main fault are  $13^\circ$  and  $25^\circ$  with branching angles  $\theta$  of  $+15^\circ$  and  $+30^\circ$ . In our computations, the rupture velocities when the rupture front reached the branching point were around  $0.6v_s$  and  $0.8v_s$ . The final rupture traces of these above eight cases are the same as Figs. 12 and 13 of Kame *et al.* (2003), except for the case with an incoming rupture velocity of  $0.8v_s$ ,  $\psi$  of  $13^\circ$  and  $\theta$  of  $+30^\circ$ . In Kame *et al.* (2003), the rupture for those conditions propagates on both the main and branch faults. In our simulations, however, the rupture propagates only on the main fault, similar to the case with an incoming rupture velocity of  $0.6v_s$ . If we increase the incoming rupture velocity to  $0.9v_s$ , the rupture propagates on both the main and branch faults. We noted that the conditions that cause a rupture to propagate on both faults are very delicate, and might depend on the rupture initiation. Thus, our rupture propagation paths are slightly different from those of Kame *et al.* (2003).

As described above, we confirmed that our numerical code works properly.

## 2.5 Parameters for simulations

We considered the four cases where the dip angle of the main fault  $\psi$  is either  $13^\circ$  or  $25^\circ$  with a branching angle  $\theta$  of either  $15^\circ$  or  $30^\circ$  (Fig. 1, Table 2). Fig. 5 shows the pre-stress state we used for all four cases, which is the same as that used by Kame *et al.* (2003). We assume that  $\sigma_{n0}^{\text{eff}}$  and  $\tau_0$  on the main fault are 100 and 24 MPa, respectively, for all cases. The values of  $\sigma_{n0}^{\text{eff}}$  and  $\tau_0$  on the branch faults depend on both  $\psi$  and  $\theta$  (see Fig. 5 for details). The rupture

**Table 2.** Simulation parameters for fault geometry.

	$\psi$ ( $^\circ$ )	$\theta$ ( $^\circ$ )	$L$ (km)	$L_1$ (km)	$L_2$ (km)
Model 1	13	15	12	-5.925	6.075
Model 2	13	30	13	-5.025	7.975
Model 3	25	15	12	-7.050	4.950
Model 4	25	30	12	-6.225	5.775

Note:  $\psi$ ,  $\theta$ ,  $L$ ,  $L_1$  and  $L_2$  are defined in Fig. 1.

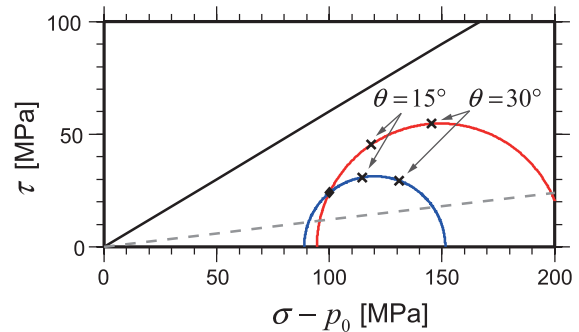


**Figure 5.** Stress field in the cases with the dip angles of the main fault  $\psi$  of  $13^\circ$  (red curves) and  $25^\circ$  (blue curves). The diamond and crosses indicate the initial stresses on the main and branch faults, respectively. Note that the effective stresses are shown. The effective maximum principal stress  $\sigma_{\text{max}}^{\text{eff}} = \sigma_{\text{max}} - p_0$  and the effective minimum principal stress  $\sigma_{\text{min}}^{\text{eff}} = \sigma_{\text{min}} - p_0$  are 203.96 and 94.46 MPa, respectively, when  $\psi$  is  $13^\circ$ .  $\sigma_{\text{max}}^{\text{eff}}$  and  $\sigma_{\text{min}}^{\text{eff}}$  are 151.47 and 88.81 MPa, respectively, when  $\psi$  is  $25^\circ$ . The solid black and dashed grey lines show the Coulomb fracture criterion ( $\mu_s \sigma_n^{\text{eff}}$ ) and the friction level ( $\mu_d \sigma_n^{\text{eff}}$ ), respectively.

**Table 3.** Simulation parameters for dynamic ruptures.

Property	Symbol	Value
Density	$\rho$	2670 kg m <sup>-3</sup>
<i>P</i> -wave velocity	$v_p$	6.000 km s <sup>-1</sup>
<i>S</i> -wave velocity	$v_s$	3.464 km s <sup>-1</sup>
Grid spacing	$\Delta x_1$	
In the absence of TP		25.0 m
With TP		6.25 m
Time step	$\Delta t$	
In the absence of TP		1.8 × 10 <sup>-3</sup> s
With TP		4.5 × 10 <sup>-4</sup> s
Time collocation parameter <sup>a</sup>	$e_t$	0.9
Static coefficient of friction	$\mu_s$	0.60
Dynamic coefficient of friction	$\mu_d$	0.12
Characteristic displacement	$D_c$	0.64 m

<sup>a</sup> $e_t$  is introduced by Tada & Madariaga (2001).

initiation is the same in all cases. The length of the nucleation patch is 1.0 km and the initial shear stress inside the nucleation patch is  $\tau_s + 2.0$  MPa. TP is not in effect inside the nucleation patch regardless of whether or not it is in effect on the main fault. The distance from the nucleation patch to the branching intersection is 1.9 km. The rupture velocity when the rupture front reaches the branching point is about  $0.6v_s$  for the cases where TP is not in effect.

Tables 1 and 3 list the parameters used in this study. Ujiie *et al.* (2007) observed that ultracataclasite in an ancient subduction thrust is mostly a few centimetres thick, so the value of  $w$  in our simulations (1 cm) is reasonable. Permeability  $k$  and porosity  $\phi$  for the sediments of four different subduction zones ranges from  $10^{-19}$  to  $10^{-15}$  m<sup>2</sup> and from 0.2 to 0.9, respectively, at effective stress of up to 12.4 MPa (Gamage *et al.* 2011). We set  $k$  at  $5 \times 10^{-17}$  m<sup>2</sup> and  $\phi$  at 0.025, which is smaller than the measured values of  $\phi$ . Our choices are still reasonable because  $k$  and  $\phi$  are found to decrease dramatically with increasing effective stress (e.g. Tanikawa & Shimamoto 2009; Ikari & Saffer 2012), which could be larger in seismogenic conditions than 12.4 MPa of the measurements. If we use a larger value of  $\phi$ , TP would be more effective because the hydraulic diffusivity  $\omega = k/\eta\beta_r\phi$  is proportional to  $k/\phi$ . From the values in Table 1,  $\omega$  is approximately  $10^{-2}$  m<sup>2</sup> s<sup>-1</sup>, much larger than the thermal diffusivity  $\chi = 10^{-6}$  m<sup>2</sup> s<sup>-1</sup>. Therefore,  $\omega$  dominates TP's effect (eq. 2).

We assumed  $\mu_s$  to be 0.6, consistent with laboratory experiments using fault gouge from the megasplay fault zone in the Nankai subduction zone (Ujiie & Tsutsumi 2010). The  $S$  value in the absence of TP, as defined by Andrews (1976), is set at 3.0 on the main fault.  $D_c$  is 0.64 m, consistent with seismic observations for strike-slip earthquakes (Mikumo *et al.* 2003; Fukuyama & Mikumo 2007).

### 3 RESULTS

#### 3.1 Low main fault dip angle ( $\psi = 13^\circ$ )

First, we will describe the dynamic rupture branching behaviour calculated for a main fault dip angle  $\psi$  of  $13^\circ$  and a branch angle  $\theta$  of  $15^\circ$  (Model 1 in Table 2). Fig. 6(a) shows the evolution of slip velocity on the main and branch faults when TP is not in effect on either fault. The rupture initiated on the main fault propagates bilaterally along the main fault. After the rupture encounters the intersection, it terminates. A rupture on the branch fault, however, is triggered and propagates successfully. Thus, the rupture propagates along the branch fault.

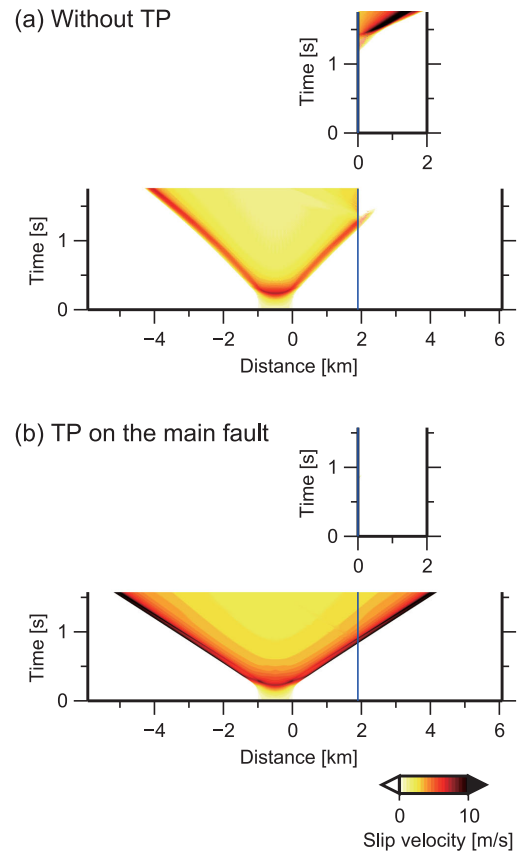


**Figure 6.** Time history of the slip velocity along the main (lower panel) and branch (upper panel) faults. The dip angle of the main fault  $\psi$  is  $13^\circ$  and the branching angle  $\theta$  is  $15^\circ$  (Model 1 in Table 2). (a) TP is not in effect on either of the faults and (b) TP is in effect only on the main fault. The blue lines show the branch intersection. Note that the blue lines in the bottom panels do not indicate the edge of the main fault.

TP can alter the rupture propagation paths. Fig. 6(b) shows the time history of the slip velocity when TP is in effect only on the main fault. TP increases the slip velocity and the rupture velocity on the main fault, as described by previous numerical studies (e.g. Bizzarri & Cocco 2006a,b; Bizzarri & Spudich 2008; Urata *et al.* 2008, 2012). In this case, the rupture on the main fault continues to propagate after encountering the branch point. A rupture on the branch is triggered, but it immediately dies out. Due to TP on the main fault, the rupture propagates along the main fault. However, when TP is in effect on both the main and branch faults, the rupture propagates along the branch (Fig. 7a).

The rupture propagation paths depend on the branch angle  $\theta$  when TP is not in effect on either fault (Fig. 7; Kame *et al.* 2003). The rupture propagates along the branch fault in Model 1 ( $\theta = 15^\circ$ ; Figs 6a and 7a), but along the main fault in Model 2 ( $\theta = 30^\circ$ ; Fig. 7b). The rupture propagation paths, however, do not depend on the branch angle  $\theta$  when TP is in effect. Ruptures propagate along the main fault in cases with TP on the main fault, and along the branch fault when TP is in effect on both faults (Fig. 7). This is observed in both Models 1 ( $\theta = 15^\circ$ ) and 2 ( $\theta = 30^\circ$ ). Thus, dynamic rupture processes are affected more strongly by TP than by  $\theta$ .

Why does TP alter rupture propagation paths? Rupture propagation paths are controlled by the pre-stress state when TP is not in effect on either fault. Fig. 8 shows the distribution of stress

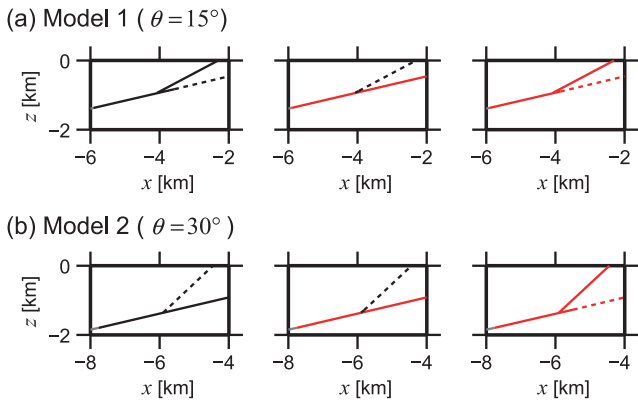


**Figure 7.** Final rupture traces in the vicinity of the branch intersection when (a) the branching angle  $\theta$  is  $15^\circ$  (Model 1) and (b)  $30^\circ$  (Model 2). The solid lines indicate that rupture propagated and the dashed lines indicate that rupture did not propagate. The grey lines show the nucleation patch. The red and black lines correspond to the faults with and without TP, respectively.

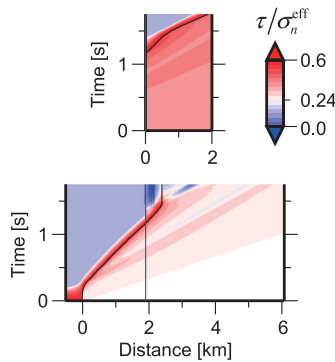
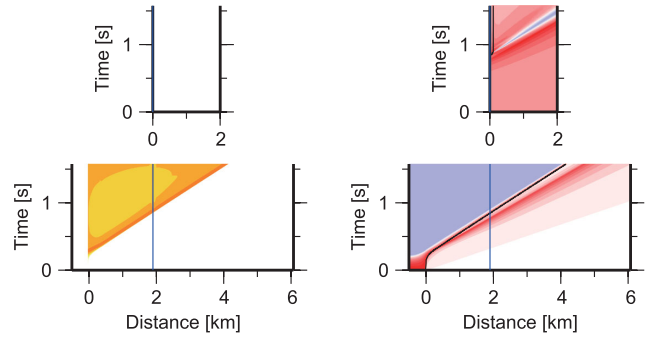


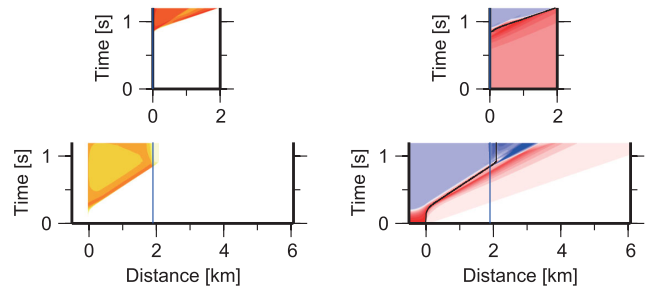
**Figure 8.** Time history of the stress ratio  $\tau/\sigma_n^{\text{eff}}$  along the main (lower panel) and branch (upper panel) faults when TP is not in effect on either fault. The dip angle of the main fault  $\psi$  is  $13^\circ$  and the branching angle  $\theta$  is  $15^\circ$  (Model 1). The white colour corresponds to the initial value on the main fault (0.24). The red and blue colours indicate  $\tau/\sigma_n^{\text{eff}}$  values higher and lower than 0.24, respectively. During slips,  $\tau/\sigma_n^{\text{eff}}$  obeys the slip-weakening law (Fig. 2). The black curves indicate the evolution of the rupture front. The dark blue regions at distances of 1.9–2.3 km on the main fault, which appear after the rupture front arrives, show that the slip arrests and that  $\tau/\sigma_n^{\text{eff}}$  no longer obeys the slip-weakening law. The blue lines show the branch intersection.

ratio  $\tau/\sigma_n^{\text{eff}}$  in Model 1 ( $\theta = 15^\circ$ ). The stress ratio increases on both faults owing to slip on the main fault before the rupture encounters the branch intersection, and ruptures on both faults are triggered. The rupture triggered on the branch fault is more likely to propagate because the pre-stress state on the branch fault is closer to the Coulomb failure criterion than on the main fault in Model 1 ( $\theta = 15^\circ$ ; Fig. 5). Once the rupture propagates, the stress shadow (Yamashita & Umeda 1994) of the branch fault, which corresponds to the blue regions in Fig. 8 at distances of 2.5–3.5 km on the main fault, hinders rupture propagation along the main fault. Although in Model 2 ( $\theta = 30^\circ$ ; Fig. 5), the pre-stress state on the branch is a little closer to the Coulomb failure criterion than that on the main fault, the fracture energy  $G_c = \frac{1}{2}(\mu_s - \mu_d)\sigma_{n0}^{\text{eff}}D_c$  is much higher (solid and dashed lines in Fig. 5), and thus the rupture propagates along the main fault. When TP is in effect on the main fault, the increase in pore pressure (left-hand panel in Fig. 9a) rapidly weakens the shear resistance, promoting rupture on the main fault. A large, quick stress drop promotes the stress shadow effect (right-hand panel in Fig. 9a),

(a) TP on the main fault (Model 1)



(b) TP on both faults (Model 1)



(c) TP on both faults (Model 3)

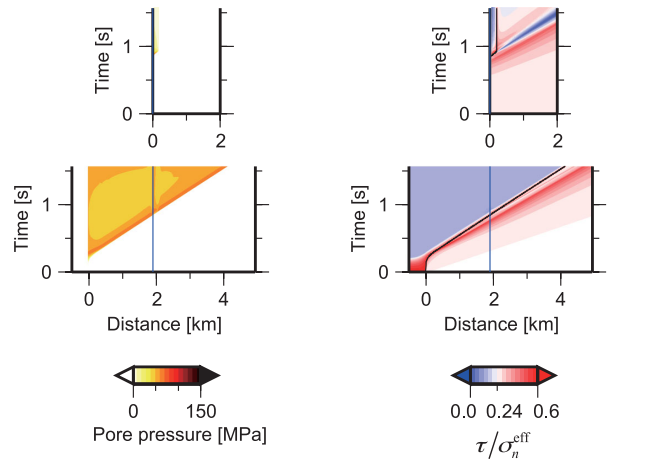


**Figure 9.** Time history of pore pressure change  $\Delta p$  (left-hand panels) and stress ratio  $\tau/\sigma_n^{\text{eff}}$  (right-hand panels) (a) when TP is in effect only on the main fault in the case with  $\psi$  of  $13^\circ$  (Model 1), (b) when TP is in effect on both faults in the case with  $\psi$  of  $13^\circ$  (Model 1), and (c) when TP is in effect on both faults in the case with  $\psi$  of  $25^\circ$  (Model 3). The branching angle  $\theta$  is  $15^\circ$ . The upper and lower panels correspond to the branch and main faults, respectively. The blue lines show the branch intersection. The right-hand panels are drawn in the same manner as Fig. 8. Dark blue regions at distances of 1.9–2.1 km on the main fault in the right-hand panel of (b) and at distances of 0–0.2 km on the branch fault in the right-hand panel of (c) indicate that the slip arrests and that  $\tau/\sigma_n^{\text{eff}}$  no longer obeys the slip-weakening law.

suppressing rupture propagation on the branch fault. When TP is in effect on both faults, the rupture propagation paths are controlled by the TP's effectiveness. TP on the branch fault is more effective and the pore pressure on the branch fault increases much more than on the main fault (left-hand panel in Fig. 9b). The effective TP on the branch fault results from high initial normal and shear stresses (Fig. 5). The high initial stresses increase frictional heating, and

the high initial shear stress can increase the stress drop if TP is in effect. The TP on the branch fault encourages rupture propagation on the branch fault and enhances the stress shadow effect (right-hand panel in Fig. 9b). As a result, the rupture propagates along the branch fault.

### 3.2 High main fault dip angle ( $\psi = 25^\circ$ )

The initial stresses on the branch faults are different at  $\psi$  values of  $13^\circ$  and  $25^\circ$ , although the initial stresses on the main fault are the same (Fig. 5). Therefore, the dynamic ruptures are the same before the rupture front reaches the branching intersection, but the dynamic fault branching is different. When  $\psi$  is  $25^\circ$ , the rupture propagates along the main fault for both Models 3 ( $\theta = 15^\circ$ ) and 4 ( $\theta = 30^\circ$ ), whether or not TP is in effect. The pre-stress state on the main fault is closer to the Coulomb failure criterion than on the branch faults, and the fracture energy  $G_c$  of the main fault is smaller than that of the branch faults (Fig. 5), so the main fault is more likely to break. In addition, TP on the branch fault is less effective than when  $\psi$  is  $13^\circ$ . Fig. 9(c) shows that the increase in the pore pressure on the branch fault is small and that the rupture propagates along the main fault even when TP is in effect on both faults.

### 3.3 Free surface effect

We considered the case where a free surface is located 20 m above the faults' upper edge. Appendix A details the numerical method we employed. It should be noted that full-space and half-space computations are the same until the reflected waves from the free surface arrive at the branch fault system. However, once the reflected waves from the free surface arrive, they change the stress field and thus alter the slips on the faults. We examined cases where the dip angle of the main fault  $\psi$  is  $13^\circ$  with a branching angle  $\theta$  of  $15^\circ$ , with TP in effect and not in effect on the main fault. Please note that TP is not in effect on the branch.

When TP is not in effect on either of the faults, the behaviour of the dynamic rupture branching is similar to the case without the free surface: the rupture propagates along the branch fault and the stress shadow effect hinders the rupture from propagating along the main fault. In contrast, when TP is in effect on the main fault, the free surface alters the rupture propagation path. Fig. 10(a) shows the slip velocity on both faults. First, the rupture propagates along the main fault. This is also observed when there is no free surface (Fig. 6b). During rupture propagation along the main fault, seismic waves reflected at the free surface arrive at both faults (Fig. 10b). Then, the reflected waves trigger rupture near the centre of the branch fault, and the rupture propagates bilaterally (Fig. 10a). Slip on the branch fault suppresses slip on the main fault (the white regions shown after 1.5 s at distances of 2.0–3.5 km on the main fault in Fig. 10a). Therefore, the rupture finally propagates along both faults because of the free surface and TP on the main fault.

It should be noted that the asymmetric pattern of slip velocity distribution in Fig. 10(a) results from the inclination of the main fault with respect to the free surface. The figure shows that the traveltimes of reflected  $S$  waves emitted from the nucleation patch (Fig. 10b) are well correlated with the spatiotemporal variation of slip velocity (Fig. 10a). The arrival of the reflected  $S$  waves changed the stress field and promoted slips behind the crack tip. It should also be kept in mind that the slip velocity on the faults is also affected by the reflected waves emitted from the propagating crack.

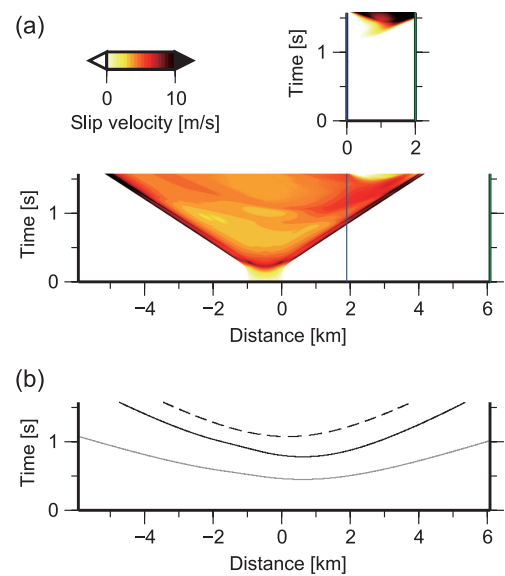


**Figure 10.** (a) Time history of slip velocity along the main (lower panel) and branch (upper panel) faults when a free surface exists and (b) the arrival time of  $P$  and  $S$  waves emitted from the nucleation patch and reflected at the free surface. The dip angle of the main fault  $\psi$  is  $13^\circ$  and the branching angle  $\theta$  is  $15^\circ$ . TP is in effect only on the main fault. (a) The blue vertical lines show the branch intersection. The green lines indicate the points closest to the free surface. (b) The grey and black solid lines are arrival times of  $pP$  and  $sS$  phases radiated from the nucleation patch at 0 s. The dashed line shows the arrival time of  $sS$  radiated from the centre of the nucleation patch (a distance of  $-0.5$  km) at 0.23 s when the slip velocity at a distance of  $-0.5$  km is at its maximum.

## 4 DISCUSSION

### 4.1 Implications for the Nankai subduction zone

Large interplate earthquakes have occurred repeatedly along the Nankai subduction zone off the coast of southwest Japan (Ando 1975), accompanied by disastrous tsunamis, most recently in 1944 (the Tonankai earthquake) and 1946 (the Nankai earthquake). Tsunami data suggested possible coseismic slips on splay faults during both earthquakes (Cummins & Kaneda 2000; Baba *et al.* 2006), although the resolution of seismic and tsunami waveforms was not fine enough to distinguish whether slip was dominant on the splay fault or on the plate interface. Seismic reflection data along the Nankai subduction zone suggested that there is a megasplay fault that runs continuously from the plate interface to the surface and cuts the old thrust faults within the frontal accretionary prism (Moore *et al.* 2007). From this, Moore *et al.* (2007) speculated that the megasplay fault was active during the 1944 Tonankai earthquake. Recently, the Integrated Ocean Drilling Program (IODP) Nankai Trough Seismogenic Zone Experiment (NanTroSEIZE; Tobin & Kinoshita 2006) drilled and cored several holes in the shallow portions of the megasplay and frontal plate boundary faults. Vitrinite reflectance geothermometry revealed that both fault zones experienced localized temperatures of more than  $380^\circ\text{C}$ , implying that coseismic slip would have propagated at least once to the updip end of the megasplay fault and to the toe of the accretionary wedge (Sakaguchi *et al.* 2011).

Tanikawa *et al.* (2012) measured the permeability of the core materials from the megathrust and frontal thrust of the Nankai subduction zone before and after sliding friction tests. They showed that the permeability of the splay fault materials under wet conditions

is higher than that of the frontal thrust materials before the friction test, but the permeability of both fault materials decreases to around  $10^{-19} \text{ m}^2$  at a confining pressure of 3.5 MPa. These measurements imply that TP could be more effective on the frontal thrust than on the splay fault when the splay fault has not experienced a large slip, and that TP could be in effect on both frontal and thrust faults when the splay fault has experienced slips. Combining these implications with our results for cases with a small main fault dip angle ( $\psi = 13^\circ$ ; Fig. 7), we can envision the following scenarios: the rupture may propagate along the frontal thrust in the former case, but may propagate along the splay fault in the latter case. These implications are consistent with previous studies that suggested that the both splay and frontal thrusts would have slipped coseismically at least once (Sakaguchi *et al.* 2011) and that seismic slip could have occurred on the splay fault during the most recent event (Moore *et al.* 2007).

#### 4.2 Validity of our results

The element size  $\Delta x_1$  and the time step  $\Delta t$  in our simulations (Table 3) are sufficiently small so as not to change our results. The effects of  $\Delta x_1$  and  $\Delta t$  are described in detail in Appendix B.

We assumed that fluid migration between the main and branch faults does not affect each other. This assumption is reasonable in our simulations. Since the hydraulic diffusivity  $\omega$  is  $\omega \approx 10^{-2} \text{ m}^2 \text{ s}^{-1}$  (Section 2.5), the pore pressure diffusion length  $2\sqrt{\omega t}$  is 0.2 m for  $t = 1 \text{ s}$ . This is quite small compared to the element dimension, so the effect of fluid migration can indeed be ignored.

To investigate whether or not melting would occur during a rupture, we calculated the temperature increase due to frictional heating. We examined Model 1 in full-space without a free surface. We assumed that the temperature change at location  $\mathbf{x}$  on the fault surface obeys the following equation (Bizzarri & Cocco 2006a):

$$\Delta T(\mathbf{x}, t) = \frac{1}{c_w} \int_0^{t-\epsilon} dt' \cdot \text{erf} \left[ \frac{w}{4\sqrt{\chi(t-t')}} \right] \tau(\mathbf{x}, t') v(\mathbf{x}, t'), \quad (4)$$

in the same way as pore pressure change (eq. 2). In both cases, where TP is in effect on only the main fault and where it is in effect on both faults, the temperature increase does not exceed  $900 \text{ }^\circ\text{C}$  during the calculated time period (Figs 9a and b), except in and near the nucleation patch. If the melting temperature is approximately  $1000 \text{ }^\circ\text{C}$  and the initial temperature is lower than  $100 \text{ }^\circ\text{C}$ , which corresponds to the temperature 3 to 4 km deep, melting will not occur except in and near the nucleation patch. The temperature increase is high in the nucleation patch because we assumed that TP is not in effect there so that the nucleation processes are the same in all cases. TP lowers the temperature increase, preventing melting, as suggested by Sibson (1973).

In half-space cases, the rupture processes may differ depending on the depth of the fault intersection point because the time until the reflected waves trigger the rupture on the branch fault varies with depth. The results shown in Section 3.3 might not change qualitatively despite this variability.

In this study, we assumed uniform external stresses, while Kitajima & Saffer (2012) suggested that effective stress increases with distance from the trench axis by combining  $P$ -wave velocities obtained from geophysical surveys with empirical relationships between  $P$ -wave velocity, porosity, and effective mean stress defined by laboratory deformation tests on drill core samples of oceanic sediment. We also ignored the hydraulic fracturing that might be caused by increased pore pressure due to TP that was suggested by Ujiie *et al.* (2007). We assumed constant porosity, but dilatancy,

which is an increase in pore space caused by fault slips, can affect dynamic ruptures (e.g. Bizzarri 2012 and references cited therein). These effects could be included for more realistic simulations in future work. We assumed the linear slip-weakening law (eq. 1). The slip-weakening law represents physically reasonable features in dynamic ruptures, along with other fault governing models (reviewed by Bizzarri 2011). We focused on 2-D mode II (in-plane) ruptures in this study. Our results would be still reasonable if the fault width along the trough axis is small in 3-D geometry. If the fault width is long, the mode III (anti-plane) component should be taken into account.

## 5 CONCLUSIONS

We performed a series of numerical simulations of dynamic fault branching including TP, based on the branch fault model of Kame *et al.* (2003). We revealed that TP can alter rupture propagation paths when the dip angle of the main fault is small. The rupture propagation paths depend on the branching angle when TP is not in effect on either of the faults. In contrast, the rupture propagates along the main fault in cases where TP is in effect on the main fault, but along the branch when TP is in effect on both faults. These features occur regardless of the branching angle. Thus, dynamic rupture processes are controlled more strongly by TP than by the branching angle. Finally, we considered the case when there is a free surface above the branch fault system. In this case, the rupture can propagate along both faults because of the combination of the free surface and TP on the main fault.

## ACKNOWLEDGEMENTS

This work was supported by the JST J-Rapid/ANR FLASH-Japan DYNTOHOKU project (ANR-11-JAPN-0009), the NIED project for Development of Monitoring and Forecasting Technology for Crustal Activity, and the NIED joint project with JAMSTEC on High Frequency Source Modelling. Two anonymous reviewers' comments were quite valuable in improving our manuscript. Professors Sánchez-Sesma and Iturrarán-Viveros kindly provided their computation code for the Garvin solution. Generic Mapping Tool (GMT version 4.5.6, Wessel & Smith 1998) software was used to draw some of the figures.

## REFERENCES

- Ando, M., 1975. Source mechanisms and tectonic significance of historical earthquakes along the Nankai trough, Japan, *Tectonophysics*, **27**, 119–140.
- Andrews, D.J., 1976. Rupture velocity of plane strain shear cracks, *J. geophys. Res.*, **81**, 5679–5689.
- Andrews, D.J., 2002. A fault constitutive relation accounting for thermal pressurization of pore fluid, *J. geophys. Res.*, **107**, 2363, doi:10.1029/2002JB001942.
- Aochi, H. & Fukuyama, E., 2002. Three-dimensional nonplanar simulation of the 1992 Landers earthquake, *J. geophys. Res.*, **107**, 2035, doi:10.1029/2000JB000061.
- Archuleta, R., 1984. A fault model for the 1979 Imperial Valley earthquake, *J. geophys. Res.*, **89**, 4559–4585.
- Baba, T., Cummins, P.R., Hori, T. & Kaneda, Y., 2006. High precision slip distribution of the 1944 Tonankai earthquake inferred from tsunami waveforms: possible slip on a splay fault, *Tectonophysics*, **426**, 119–134.
- Bhat, H.S., Dmowska, R., Rice, J.R. & Kame, N., 2004. Dynamic slip transfer from the Denali to Totschunda faults, Alaska: testing theory for fault branching, *Bull. seism. Soc. Am.*, **94**, 202–213.

- Bhat, H.S., Olives, M., Dmowska, R. & Rice, J.R., 2007. Role of fault branches in earthquake rupture dynamics, *J. geophys. Res.*, **112**, B11309, doi:10.1029/2007JB005027.
- Bizzarri, A., 2011. On the deterministic description of earthquakes, *Rev. Geophys.*, **49**, RG3002, doi:10.1029/2011RG000356.
- Bizzarri, A., 2012. Effects of permeability and porosity evolution on simulated earthquakes, *J. Struct. Geol.*, **38**, 243–253.
- Bizzarri, A. & Cocco, M., 2006a. A thermal pressurization model for the spontaneous dynamic rupture propagation on a three-dimensional fault: 1. Methodological approach, *J. geophys. Res.*, **111**, B05303, doi:10.1029/2005JB003862.
- Bizzarri, A. & Cocco, M., 2006b. A thermal pressurization model for the spontaneous dynamic rupture propagation on a three-dimensional fault: 2. Traction evolution and dynamic parameters, *J. geophys. Res.*, **111**, B05304, doi:10.1029/2005JB003864.
- Bizzarri, A. & Spudich, P., 2008. Effects of supershear rupture speed on the high-frequency content of S waves investigated using spontaneous dynamic rupture models and isochrone theory, *J. geophys. Res.*, **113**, B05304, doi:10.1029/2007JB005146.
- Collot, J.-Y., Agudelo, W., Ribodetti, A. & Marcaillou, B., 2008. Origin of a crustal splay fault and its relation to the seismogenic zone and underplating at the erosional north Ecuador–south Colombia oceanic margin, *J. geophys. Res.*, **113**, B12102, doi:10.1029/2008JB005691.
- Cummins, P.R. & Kaneda, Y., 2000. Possible splay fault slip during the 1946 Nankai earthquake, *Geophys. Res. Lett.*, **27**, 2725–2728.
- Doan, M.L., Brodsky, E.E., Kano, Y. & Ma, K.F., 2006. In situ measurement of the hydraulic diffusivity of the active Chelungpu fault, Taiwan, *Geophys. Res. Lett.*, **33**, L16317, doi:10.1029/2006GL026889.
- Fukuyama, E. & Mikumo, T., 2006. Dynamic rupture propagation during the 1891 Nobi, central Japan, earthquake: a possible extension to the branched faults, *Bull. seism. Soc. Am.*, **96**, 1257–1266.
- Fukuyama, E. & Mikumo, T., 2007. Slip-weakening distance estimated at near-fault stations, *Geophys. Res. Lett.*, **34**, L09302, doi:10.1029/2006GL029203.
- Gamage, K., Screaton, E., Bekins, B. & Aiello, I., 2011. Permeability-porosity relationships of subduction zone sediments, *Mar. Geol.*, **279**, 19–36.
- Hasegawa, A., Nakajima, J., Uchida, N., Okada, T., Zhao, D., Matsuzawa, T. & Umino, N., 2009. Plate subduction, and generation of earthquakes and magmas in Japan as inferred from seismic observations: an overview, *Gondwana Res.*, **16**, 370–400.
- Hok, S. & Fukuyama, E., 2011. A new BIEM for rupture dynamics in half-space and its application to the 2008 Iwate-Miyagi Nairiku earthquake, *Geophys. J. Int.*, **184**, 301–324.
- Ida, Y., 1972. Cohesive force across the tip of a longitudinal-shear crack and Griffith's specific surface energy, *J. geophys. Res.*, **77**, 3796–3805.
- Ikari, M.J. & Saffer, D.M., 2012. Permeability contrasts between sheared and normally consolidated sediments in the Nankai accretionary prism, *Mar. Geol.*, **295–298**, 1–13.
- Ishikawa, T. *et al.*, 2008. Coseismic fluid–rock interactions at high temperatures in the Chelungpu fault, *Nat. Geosci.*, **1**, 679–683.
- Kame, N., Rice, J.R. & Dmowska, R., 2003. Effects of prestress state and rupture velocity on dynamic fault branching, *J. geophys. Res.*, **108**, 2265, doi:10.1029/2002JB002189.
- Kitajima, H. & Saffer, D.M., 2012. Elevated pore pressure and anomalously low stress in regions of low frequency earthquakes along the Nankai Trough subduction megathrust, *Geophys. Res. Lett.*, **39**, L23301, doi:10.1029/2012GL053793.
- Mikumo, T., Olsen, K.B., Fukuyama, E. & Yagi, Y., 2003. Stress-breakdown time and slip-weakening distance inferred from slip-velocity functions on earthquake faults, *Bull. seism. Soc. Am.*, **93**, 264–282.
- Moore, G.F., Bangs, N.L., Taira, A., Kuramoto, S., Pangborn, E. & Tobin, H.J., 2007. Three-dimensional splay fault geometry and implications for tsunami generation, *Science*, **318**, 1128, doi:10.1126/science.1147195.
- Noda, H. & Lapusta, N., 2013. Stable creeping fault segments can become destructive as a result of dynamic weakening, *Nature*, **493**, 518–521.
- Oglesby, D.D., Day, S.M., Li, Y.-G. & Vidale, J.E., 2003. The 1999 Hector Mine earthquake: the dynamics of a branched fault system, *Bull. seism. Soc. Am.*, **93**, 2459–2476.
- Okada, Y., 1992. Internal deformation due to shear and tensile faults in a half-space, *Bull. seism. Soc. Am.*, **82**, 1018–1040.
- Park, J.-O., Tsuru, T., Kodaira, S., Cummins, P.R. & Kaneda, Y., 2002. Splay fault branching along the Nankai subduction zone, *Science*, **297**, 1157–1160.
- Poliakov, A.N.B., Dmowska, R. & Rice, J.R., 2002. Dynamic shear rupture interactions with fault bends and off-axis secondary faulting, *J. geophys. Res.*, **107**, 2295, doi:10.1029/2001JB000572.
- PROPATH Group, 2008. PROPATH: A Program Package for Thermophysical Properties, version 13.1.
- Sakaguchi, A. *et al.*, 2011. Seismic slip propagation to the updip end of plate boundary subduction interface faults: vitrinite reflectance geothermometry on Integrated Ocean Drilling Program NanTro SEIZE cores, *Geology*, **39**, 395–398.
- Sánchez-Sesma, F.J. & Iturrarán-Viveros, U., 2006. The classic Garvin's problem revisited, *Bull. seism. Soc. Am.*, **96**, 1344–1351.
- Sibson, R.H., 1973. Interactions between temperature and pore-fluid pressure during earthquake faulting and a mechanism for partial or total stress relief, *Nat. Phys. Sci.*, **243**, 66–68.
- Sibson, R.H., 1977. Kinetic shear resistance, fluid pressures and radiation efficiency during seismic faulting, *Pure appl. Geophys.*, **115**, 387–400.
- Sibson, R.H., 1986. Brecciation processes in fault zones: inferences from earthquake rupturing, *Pure appl. Geophys.*, **124**, 159–175.
- Sieh, K. *et al.*, 1993. Near-field investigations of the Landers earthquake sequence, April to July 1992, *Science*, **260**, 171–176.
- Tada, T. & Madariaga, R., 2001. Dynamic modelling of the flat 2-D crack by a semi-analytic BIEM scheme, *Int. J. Numer. Meth. Engng.*, **50**, 227–251.
- Tamura, S. & Ide, S., 2011. Numerical study of splay faults in subduction zones: the effects of bimaterial interface and free surface, *J. geophys. Res.*, **116**, B10309, doi:10.1029/2011JB008283.
- Tanikawa, W. & Shimamoto, T., 2009. Frictional and transport properties of the Chelungpu fault from shallow borehole data and their correlation with seismic behavior during the 1999 Chi-Chi earthquake, *J. geophys. Res.*, **114**, B01402, doi:10.1029/2008JB005750.
- Tanikawa, W., Mukoyoshi, H., Tadai, O., Hirose, T., Tsutsumi, A. & Lin, W., 2012. Velocity dependence of shear-induced permeability associated with frictional behavior in fault zones of the Nankai subduction zone, *J. geophys. Res.*, **117**, B05405, doi:10.1029/2011JB008956.
- Tobin, H.J. & Kinoshita, M., 2006. NanTroSEIZE: the IODP Nankai Trough seismogenic zone experiment, *Sci. Drill.*, **2**, 23–27.
- Tsuji, T., Kawamura, K., Kanamatsu, T., Kasaya, T., Fujikura, K., Ito, Y., Tsuru, T. & Kinoshita, M., 2013. Extension of continental crust by anelastic deformation during the 2011 Tohoku-oki earthquake: the role of extensional faulting in the generation of a great tsunami, *Earth plan. Sci. Lett.*, **364**, 44–58.
- Ujije, K. & Tsutsumi, A., 2010. High-velocity frictional properties of clay-rich fault gouge in a megasplay fault zone, Nankai subduction zone, *Geophys. Res. Lett.*, **37**, L24310, doi:10.1029/2010GL046002.
- Ujije, K., Yamaguchi, A., Kimura, G. & Toh, S., 2007. Fluidization of granular material in a subduction thrust at seismogenic depths, *Earth planet. Sci. Lett.*, **259**, 307–318.
- Urata, Y., Kuge, K. & Kase, Y., 2008. Heterogeneous rupture on homogeneous faults: three-dimensional spontaneous rupture simulations with thermal pressurization, *Geophys. Res. Lett.*, **35**, L21307, doi:10.1029/2008GL035577.
- Urata, Y., Kuge, K. & Kase, Y., 2012. Spontaneous dynamic rupture propagation beyond fault discontinuities: effect of thermal pressurization, *Bull. seism. Soc. Am.*, **102**, 53–63.
- Wesnowsky, S.G., 1988. Seismological and structural evolution of strike-slip faults, *Nature*, **335**, 340–343.
- Wessel, P. & Smith, W.H.F., 1998. New, improved version of Generic Mapping Tools released, *EOS, Trans. Am. geophys. Un.*, **79**, 579, doi:10.1029/98EO00426.
- Yamashita, T. & Umeda, Y., 1994. Earthquake rupture complexity due to dynamic nucleation and interaction of subsidiary faults, *Pure appl. Geophys.*, **143**, 89–116.

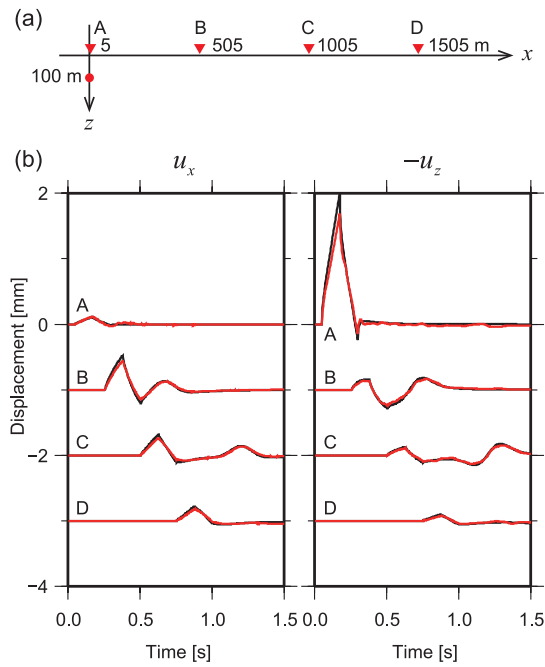


**Figure A1.** Comparison of displacement waveforms at a free surface calculated by the BIEM (red lines) and by the analytic solutions (black lines; Sánchez-Sesma & Iturrarán-Viveros 2006). (a) Model configuration. An explosive source is 100 m below the surface at  $x = 0$  m. The triangles indicate the locations of surface receivers. (b) The left- and right-hand panels show the horizontal displacement  $u_x$  and the vertical displacement  $-u_z$ , respectively.

## APPENDIX A: NUMERICAL METHOD FOR THE FREE SURFACE

The free surface was implemented in the code in the same way Hok & Fukuyama (2011) performed their 3-D BIEM. We used the kernels for full space derived by Tada & Madariaga (2001). In order to simulate a half-space, an interface composed of slipping crack elements was added at the location of the free surface, with a traction-free boundary condition as a constitutive relation. In practice, on the free surface elements, instead of solving eq. (1) for the fault elements, the following condition is solved:

$$\begin{cases} \tau = 0 \\ \sigma_n^{\text{eff}} = 0 \end{cases}, \quad (\text{A1})$$

where  $\tau$  is the shear stress and  $\sigma_n^{\text{eff}}$  is the effective normal stress. For each element, these equations are solved together with the BIEM kernels, in which the instantaneous slip velocity and the past time step loading can be separated. This leads to correct estimations of the surface motion as a response to the previous time step loading. On the fault elements, stress and slip velocity are estimated step by step. It should be noted that on the free surface elements, since the stresses are given, the free parameters are displacements in three directions.

To validate the 2-D implementation, we computed the Garvin's problem as described by Sánchez-Sesma & Iturrarán-Viveros (2006). This 2-D problem consists of placing an explosive line source 100 m below the surface to generate planar  $P$  and Rayleigh waves propagating at the surface. As we cannot generate a strictly explosive source, we use two perpendicular opening cracks; each is 0.5 m long. Fig. A1 shows synthetic seismograms for four surface receivers. The model parameters are the same as those used in fig.

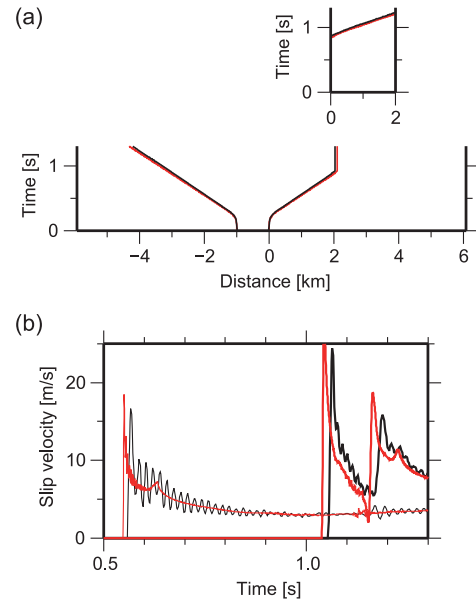


**Figure B1.** Comparison of solutions using fine grids ( $\Delta x_1 = 6.25$  m and  $\Delta t = 4.5 \times 10^{-4}$  s; red lines) and coarse grids ( $\Delta x_1 = 25.0$  m and  $\Delta t = 1.8 \times 10^{-3}$  s; black lines). The dip angle of the main fault  $\psi$  is  $13^\circ$  and the branching angle  $\theta$  is  $15^\circ$ . No free surface enters the computation. TP is in effect on both faults. (a) Evolution of the rupture front along the main (lower panel) and branch (upper panel) faults. (b) The slip velocity time histories at a distance of 1.0 km on the main fault (thin lines) and at a distance of 1.0 km on the branch fault (thick lines).

5 of Sánchez-Sesma & Iturrarán-Viveros (2006): a triangular slip source with duration of 0.25 s,  $v_p$  of  $2 \text{ km s}^{-1}$ , and  $v_s$  of  $1 \text{ km s}^{-1}$ . We set the density and the maximum of slip source time function at  $1000 \text{ kg/m}^3$  and 0.5 m, respectively. The length of the surface elements and the time interval are 10 m and 0.0025 s, respectively, for the BIEM. As shown in Fig. A1(b), the waveforms computed by the BIEM and the analytic solutions by Sánchez-Sesma & Iturrarán-Viveros (2006) are quite similar. The wave amplitude for BIEM is slightly smaller than for the analytic solutions. This difference could be due to spatiotemporal discretization in BIEM. This comparison validates our computation with the free surface.

## APPENDIX B: ACCURACY OF OUR COMPUTATIONS

The element size  $\Delta x_1$  and the time step  $\Delta t$  in our simulations (Table 3) are sufficiently small so as not to change our results. To test the influence of  $\Delta x_1$  and  $\Delta t$  on our results, we computed cases with TP using the same values of  $\Delta x_1$  and  $\Delta t$  as those in the cases without TP (four times longer). We did not include the free surface in these calculations. We confirmed that the rupture propagation paths for the fine grid (Fig. 7) and coarse grid cases were all quite similar. The rupture velocity, however, was slightly larger with smaller  $\Delta x_1$  and  $\Delta t$  values (Fig. B1) because the slip-weakening curves and stress concentration near the rupture front were reproduced more precisely in the fine grid case. We decided to show the results of our computations including TP with smaller  $\Delta x_1$  and  $\Delta t$  in this paper because the slip velocity showed significantly less oscillations (Fig. B1b) than when using larger  $\Delta x_1$  and  $\Delta t$  values. Actually, the values of  $\Delta x_1$  and  $\Delta t$  in our simulations are smaller than those used in previous studies dealing with 3-D spontaneous ruptures (Bizzarri & Cocco 2006a; Urata et al. 2008).